Waveguide-based near-eye display with dual-channel exit pupil expander

Chao Ping Chen, Lantian Mi, Wenbo Zhang, Jiaxun Ye, Gang Li*

Smart Display Lab, Department of Electronic Engineering, Shanghai Jiao Tong University, Shanghai, China

* Corresponding author.

E-mail address: lixiaogang110217@hotmail.com (G. Li).

ABSTRACT

We propose a waveguide-based near-eye display featuring a dual-channel exit pupil expander, which is composed of an in-coupler, relay gratings, and an out-coupler. Unlike the conventional waveguide-based near-eye displays, whose field of views are usually non-split or partially split, our dual-channel exit pupil expander is able to evenly split the field of view into two halves. The greatest benefit of doing so is that the upper limit of field of view could be significantly increased. The design rules for all components, including the microdisplay, collimating lens, waveguide and gratings, have been studied. The refractive index and dimension of waveguide are identified as two factors that limit the field of view. In what follows, its key specifications are recapitulated. Field of view is 70° (diagonal), eye relief is 15 mm, exit pupil is 20 × 9 mm^2, modulation transfer function is above 0.591 at 30 cycle/degree, contrast ratio is 13, and distortion is 1.38%.

Keywords: Augmented reality; Near-eye display; Waveguide; Exit pupil expander; Field of view; Grating

1. Introduction

In November 2019, PricewaterhouseCoopers released a market research report titled "Seeing is believing" to foresee the economic potential of virtual reality (VR) and augmented reality (AR) over the next decade [1]. By 2030, VR and AR are going to contribute 1.5 trillion US dollars' worth of gross domestic product to the world. For both VR and AR to pull off "Seeing is believing", near-eye displays (NEDs) play the most important role. Due to an insignificant discrepancy that VR is opaque while AR is transparent, the technology roadmaps of VR and AR diverge from the very beginning. For VR, the predominant NED architectures are the simple magnifiers [2–4]. With no exceptions, all mainstream VR devices, *e.g.* Rift (Oculus), Vive (HTC) and Gear VR (Samsung), fall into this category. For AR, things are complicated. There are a diversity of architectures. Most are based on free-space combiners [5–9] and waveguides [10–23]. Few are with contact lenses [24–28]. Which category is the best? The community has yet to reach a consensus. At the time being, it seems that major players tend to vote for waveguides, especially, those with diffractive/holographic gratings to expand the exit pupil. Typical examples are HoloLens 1 [29] & 2 [30] (Microsoft), One (Magic Leap) [31], Titan (WaveOptics) [32] and Crystal50 (DigiLens) [33]. If compared with their VR counterparts, these AR devices could outrival in many aspects, like exit pupil or eyebox and form factor. But when it comes to field of view (FOV), AR devices are definitely no match for VR devices.

Despite that VR and AR set sails along different paths, they are probably heading towards the same destination. Therefore, it is legitimate to prophesy that one particular NED solution might eventually consolidate both VR and AR. In search of such a NED, we hereby present a waveguide-based NED and reveal its potential for the said purpose.

2. Design rules

2.1. Exit pupil expander

The hardcore role of exit pupil expander (EPE) is to duplicate or clone a single pupil into many. Fig. 1 outlines the plan view of dual-channel exit pupil expander, which consists of the in-coupling grating, left/right relay grating, and out-coupling grating. The in-coupling grating is supposed to coincide with the exit pupil of collimating lens. To avoid the confusion with the exit pupil at the eye relief (ER), the foregoing exit pupil is referred to as input pupil (IP) hereafter. Having two sub-gratings with their slant angles being opposite, in-coupling grating can guide the light into the waveguide towards both left and right directions or channels. For the central field, its propagation angle θ_{wg} inside the waveguide equals the critical angle θ_c of total internal reflection (TIR), as will be discussed later. Left/right relay grating, having five sub-gratings each side, rotates the optical path by the angle α (relative to x-axis) and splits the optical path five times in a row. Out-coupling grating, having a total of 10 (horizontal) by 10 (vertical) sub-gratings, couples the light out of the waveguide, thus duplicating the pupil two dimensionally. As shown in Fig. 2, where the collimating lens is generalized as a simple magnifier, center-to-center distance L_{ir}/L_{ro} between the adjacent in-coupling/relay and relay/out-coupling sub-gratings is

$$L_{ir/ro} = 2N_{TIR}Dtan\theta_{wg} \tag{1}$$

where N_{TIR} is the number of TIR and D the thickness of waveguide. For a given center-to-center distance, D is inversely proportional to N_{TIR}. Table 1 summarizes the parameters for our EPE, where $W/W_i/W_r/W_o$ and $H/H_i/H_r/H_o$ are the horizontal and vertical dimensions of waveguide/in-coupling grating/left/right relay grating/out-coupling grating, respectively.

Table 1. Parameters of exit pupil expander.

Object	Parameter	Value
Waveguide	W	48 mm
	H	27.46 mm
	D	3.02 mm
	n_{wg} (546 nm)	1.8127
	θ_{wg}	33.49°
In-coupling grating	W_i	8 mm
	H_i	4 mm
Left/right relay grating	α	60°
	W_r	20 mm
	H_r	4 mm
	L_{ir}	4 mm
Out-coupling grating	W_o	40 mm
	H_o	20 mm
	L_{ro}	8 mm

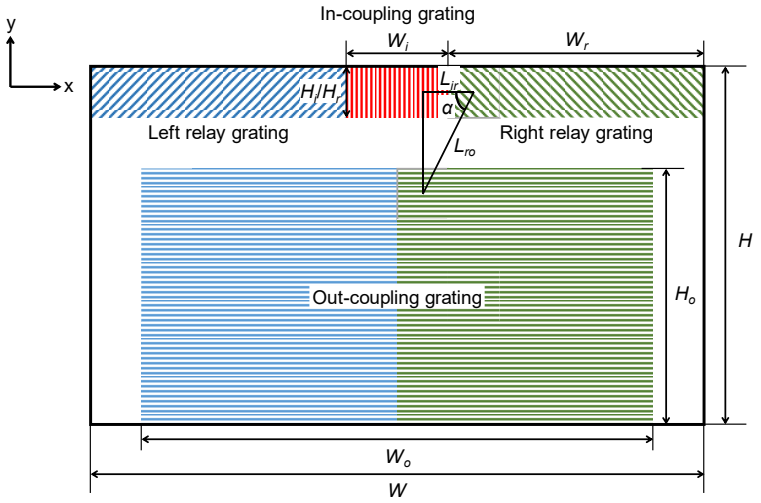

Fig. 1. Plan view of dual-channel exit pupil expander, which consists of the in-coupling grating, left/right relay grating, and out-coupling grating. Left/right relay grating, having five sub-gratings each side, rotates the optical path by the angle α (relative to x-axis) and splits the optical path five times in a row. $W/W_i/W_r/W_o$ and $H/H_i/H_r/H_o$ are the horizontal and vertical dimensions of waveguide/in-coupling grating/left/right relay grating/out-coupling grating, respectively.

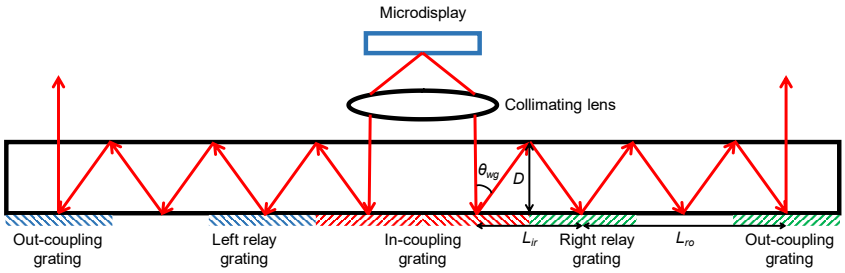

Fig. 2. Cross-section view of dual-channel exit pupil expander. The collimating lens is generalized as a simple magnifier. For the central field, its propagation angle θ_{wg} inside the waveguide equals the critical angle θ_c of total internal reflection.

2.2. k-domain

In a spherical coordinate [34], a wave vector k can be written as

$$k = (k_x, k_y, k_z) = \frac{2\pi n}{\lambda}(sin\theta cos\varphi, sin\theta sin\varphi, cos\theta) \tag{2}$$

where n is the refractive index of medium, λ the wavelength, θ the polar angle, and φ the azimuthal angle. When the medium is air, for the wave vectors emerging from a source to be able to incident to a waveguide, their polar and azimuthal angles could range from 0° to 90° and 0° to 360°, respectively. If to plot all the possible wave vectors in XY plane, as shown in Fig. 3, these wave vectors could fill up a yellow circle with a radius R_{air}

$$R_{air} = \sqrt{k_x^2(\theta = 90°) + k_y^2(\theta = 90°)} = \frac{2\pi n_{air}}{\lambda} \tag{3}$$

where n_{air} is the refractive index of air. When the medium is waveguide, for the wave vectors to be able to propagate within the waveguide, polar angles shall be greater than the critical angle θ_c of total internal reflection, *i.e.* $\theta_c < \theta < 90°$. As a result, the domain of all allowable wave vectors is represented by a green ring, whose inner and outer radii are

$$R_{in} = R_{air} \tag{4}$$

and

$$R_{wg} = \frac{2\pi n_{wg}}{\lambda} \tag{5}$$

respectively, where n_{wg} is the refractive index of waveguide. Now, consider a source emitting a finite range of wave vectors bound by a rectangular field of view (FOV) and invoke the grating equation [35] that relates the incident angle θ_{air} in air to the diffracted angle θ_{wg} in waveguide as

$$n_{air} \sin\theta_{air} - n_{wg} \sin\theta_{wg} = \frac{m\lambda}{p} \tag{6}$$

where m is the diffraction order, and p the grating period. For θ_{air} varying from FOV_{air1} to FOV_{air2} and θ_{wg} from FOV_{wg1} to FOV_{wg2}, the difference of wave vectors in both air and waveguide are identical as

$$n_{air}(sinFOV_{air1} - sinFOV_{air2}) = n_{wg}\left(sinFOV_{wg1} - sinFOV_{wg2}\right) \tag{7}$$

meaning that the area of k-domain of FOV is well conserved regardless of the medium, wavelength, grating period and diffraction order. From this conclusion, it follows that the k-domain of FOV must be containable by both yellow circle and green ring. For the case

of non-split FOV, as shown in Fig. 3(a), if $R_{wg}-R_{air} \leq 2R_{air}$, the upper limit of diagonal FOV measured in air is

$$\mathrm{FOV}_{\max} = 2\sin^{-1}\left(\frac{n_{wg}-n_{air}}{2n_{air}}\right) \tag{8}$$

If $R_{wg}-R_{air} > 2R_{air}$, $\mathrm{FOV}_{\max}$ is 180°. For the case of split FOV, as shown in Fig. 3(b), if $R_{wg}-R_{air} \leq R_{air}$, the upper limit of diagonal FOV measured in air is

$$\mathrm{FOV}_{\max} = 2\sin^{-1}\left(\frac{n_{wg}-n_{air}}{n_{air}}\right) \tag{9}$$

If $R_{wg}-R_{air} > R_{air}$, $\mathrm{FOV}_{\max}$ is 180°. Fig. 4 shows the maximum diagonal FOV with respect to the refractive index of waveguide. It can be seen that when the refractive index of waveguide is 1.8, the maximum diagonal FOVs are 47° and 106° for the non-split and split cases, respectively. When the refractive index of waveguide exceeds 3, both cases can reach their ceilings at 180°. This seems impossible or meaningless in that the waveguide—if it is flat and homogenous—cannot be infinitely large. However, for non-flat or inhomogeneous waveguides, a 180° FOV is achievable.

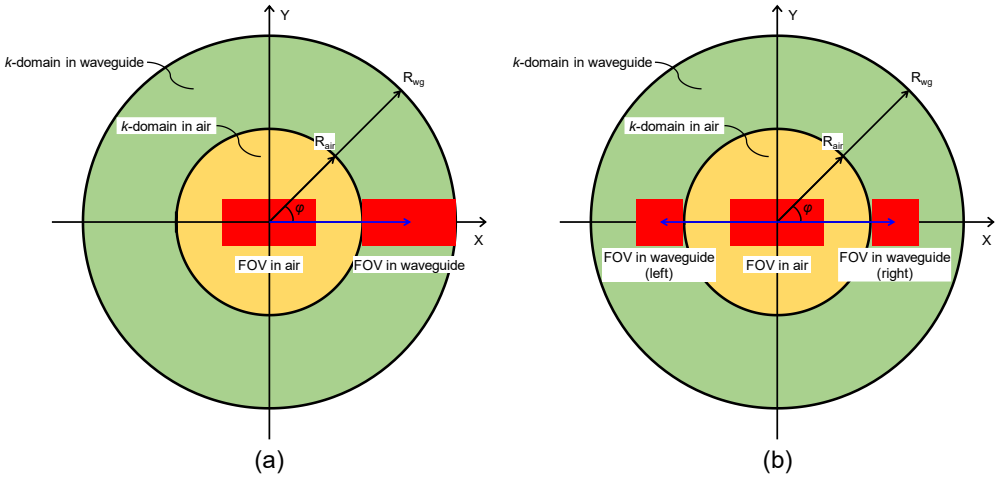

Fig. 3. Domains of all allowable wave vectors propagating in air (yellow circle) and waveguide (green ring) observed in XY plane. *k*-domains of FOV are denoted as red rectangles, which can be (a) non-split, or (b) split after entering into the waveguide.

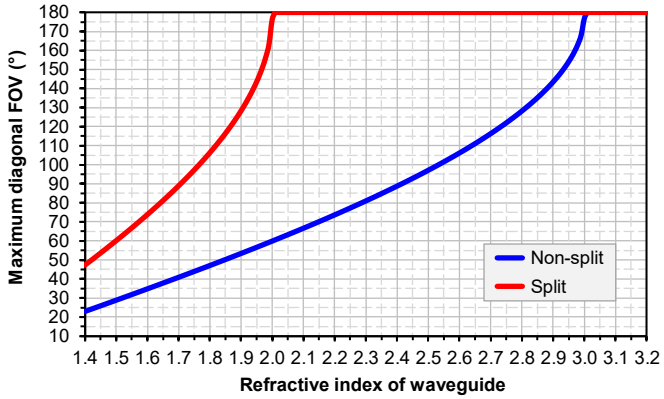

Fig. 4. Maximum diagonal FOV with respect to the refractive index of waveguide. It can be seen that when the refractive index of waveguide is 1.8, the maximum diagonal FOVs are 47° and 106° for the non-split and split cases, respectively. When the refractive index of waveguide exceeds 3, there will be no difference between two cases.

2.3. *Field of view*

For in-coupling grating, its grating equation states that

$$\frac{n_{air}\sin\theta_{in}}{n_{wg}} - \sin\theta_{wg} = \frac{m\lambda}{n_{wg}p_i} \tag{10}$$

where p_i is the grating period of in-coupling grating. For out-coupling grating, its grating equation states that

$$n_{air}\sin\theta_{out} - n_{wg}\sin\theta_{wg} = \frac{m\lambda}{p_o} \tag{11}$$

where p_o is the grating period of out-coupling grating. Subtracting Eq. (10) from Eq. (11) yields

$$n_{air}(\sin\theta_{out} - \sin\theta_{in}) = m\lambda\left(\frac{1}{p_o} - \frac{1}{p_i}\right) \tag{12}$$

When the grating periods of in-coupling and out-coupling gratings are equal, FOV can be conserved, *i.e.* FOV is decided by the projector formed by the microdisplay and collimating lens.

2.4. *Microdisplay*

For smart glasses or headsets, liquid crystal on silicon (LCoS) and organic light-emitting diode (OLED) on silicon are the two most widely adopted types of microdisplays [36]. Power consumption wise, LCoS outrivals OLED hands down. We nevertheless prefer to design with the latter for it is self-emissive, eliminating the necessity of light source and beam splitter. As an available option, ECX335S (Sony) is chosen as the microdisplay [37], the specifications of which are itemized in Table 2, where the diagonal size D_m is 0.7 inch (17.78 mm), resolution is 1920 × 1080, brightness is 3,000 nit, and contrast ratio (CR) is 100,000.

Table 2. Parameters for microdisplay.

Object	Parameter	Value
Microdisplay	D_m (diagonal)	0.7 inch (17.78 mm)
	D_m (horizontal)	15.50 mm
	D_m (vertical)	8.72 mm
	Resolution	1920 × 1080
	Brightness	3,000 nit
	CR	100,000

2.5. *Collimating lens*

As shown in Fig. 5, for the light to be perfectly collimated, the microdisplay is located at one focal length f away from the lens, thereby forming a virtual image at the infinity, whose FOV_{air} can be determined from

$$FOV_{air} = 2tan^{-1}\left(\frac{D_m}{2f}\right) \tag{13}$$

For D_m= 15.5 × 8.72 mm and f= 12.7 mm, FOV_{air}= 63° × 38°. Given the lens aperture A and lens clearance d, IP could be calculated as

$$IP = A - 2 \cdot d \cdot tan\left(\frac{FOV_{air}}{2}\right) - 2 \cdot D \cdot tan\left(\frac{FOV_{wg}}{2}\right) \tag{14}$$

where

$$FOV_{wg} = 2sin^{-1}\left(\frac{n_{air} sin(FOV_{air}/2)}{n_{wg}}\right) \tag{15}$$

For A= 9.9 × 5.2 mm, d= 0.1 mm and D= 3.02 mm, IP= 8 × 4 mm. For a quick look-up, the above parameters are itemized in Table 3.

Table 3. Parameters for collimating lens.

Object	Parameter	Value
Collimating lens	f	12.7 mm
	FOV_{air}	63° × 38°
	d	0.1 mm
	A	9.9 × 5.2 mm
	IP	8 × 4 mm

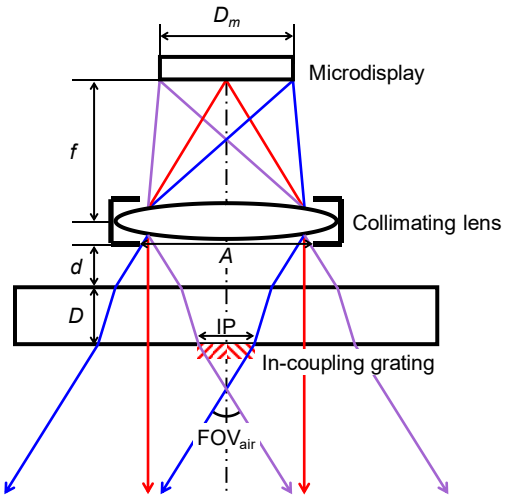

Fig. 5. Optical path diagram of microdisplay and collimating lens. D_m is the size of microdisplay, f the focal length of collimating lens, A the lens aperture, d the lens clearance, FOV_{air} the field of view measured in air, and IP the input pupil.

2.6. Achromatic cemented doublet

For the prime performance, sometimes designing a collimating lens can be intimidating [38]. That being said, a minimal design will be more desirable for wearable devices. Pursuant to this philosophy, we are in favor of achromatic cemented doublet, which comprises two lenses made from glasses with different amounts of dispersion [39]. As a rule of thumb, a common achromatic doublet is the combination of a positive lens of crown glass with large Abbe number and a negative lens of flint glass with small Abbe

number. Under first-order approximation, to zero out the net dispersion, the power of positive lens P_1 and power of negative lens P_2 should be correlated by [39]

$$P_1 + P_2 = \frac{1}{f} \tag{16}$$

and

$$\frac{P_1}{V_1} + \frac{P_2}{V_2} = 0 \tag{17}$$

where V_1 and V_2 are in turn the Abbe numbers of positive and negative lenses. Without preference, K7 (crown) and F2 (flint), both from Schott, are picked as our lens materials. Resorting to the lensmaker's equation [39], tentative parameters for the achromatic cemented doublet, which are subject to change, can be obtained as in Table 4.

Table 4. Tentative parameters for achromatic cemented doublet.

Object	Parameter	Value
Positive lens (K7)	P_1	100 m^{-1}
	refractive index @546 nm	1.5131
	V_1	60.41
	radius of curvature (front)	6.2126 mm
	radius of curvature (back)	−29.3346 mm
Negative lens (F2)	P_2	−21.260 m^{-1}
	refractive index @546 nm	1.6241
	V_2	36.37
	radius of curvature (front)	−29.3346 mm
	radius of curvature (back)	∞ mm

2.7. In-coupling grating

In-coupling grating is composed of two blazed gratings [40] with opposite directions, as depicted in Fig. 6, where h_i is the grating height, p_i the grating period, and β_i the slant angle. To couple light into the waveguide, two blazed gratings function as the reflection grating, for which the incident angle θ_i and diffraction angle θ_m of mth order—relative to the waveguide normal N_{wg}—shall obey

$$p_i(sin\theta_i - sin\theta_m) = \frac{m\lambda}{n_{wg}} \tag{18}$$

For the FOV to be bisected by the central field (θ_i= 0°), θ_m= θ_c= 2β_i. When λ= 546 nm and m= −1, then θ_m= 33.49°, β_i = 16.75°, h_i= 164.24 nm, p_i= 545.85 nm. For the FOV to be non-split or partially split, either the microdisplay can be tilted, or let θ_m> θ_c.

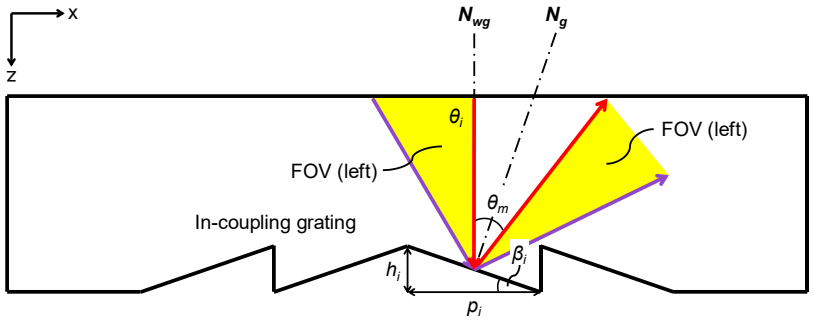

Fig. 6. Profile of in-coupling grating, which is composed of two blazed gratings with opposite directions. h_i is the grating height, p_i the grating period, β_i the slant angle, θ_i the incident angle, θ_m the diffraction angle of mth order, N_{wg} the waveguide normal, and N_g the grating normal.

2.8. Relay grating

Relay grating is constructed as rectangular or binary gratings [41], as shown in Fig. 7, where h_r is the grating height, p_r the grating period, and w_r the grating width. Referring to Fig. 8, the azimuthal angles of incident and diffracted fields differ by the angle α and the plane of incidence is inclined by the angle θ_m relative to waveguide normal N_{wg}. The incident angle θ_{ir}, diffraction angle θ_{mr} of mth order, and grating period p_r shall satisfy

$$p_r(sin\theta_{ir} - sin\theta_{mr}) = \frac{m\lambda}{n_{wg}} \tag{19}$$

where

$$\theta_{ir} = -\theta_{mr} = sin^{-1}\left(sin\theta_m sin\left(\frac{\alpha}{2}\right)\right) \tag{20}$$

When λ= 546 nm, m= +1, θ_m= 33.49° and α= 60°, θ_{ir}=−θ_{mr}= 16.02° and p_r= 545.85 nm. It is interesting to note that, in this particular case, the period of relay grating is identical to that of in-coupling grating. According to the scalar diffraction theory [42], to suppress the nonzero even orders, the fill factor needs to be 50%, *i.e.* w_r=p_r/2= 272.93 nm. Moreover, to suppress the zeroth order, the phase modulation needs to be π, *i.e.* h_r= λ/2(n_{wg}−n_{air})= 336.05 nm [42].

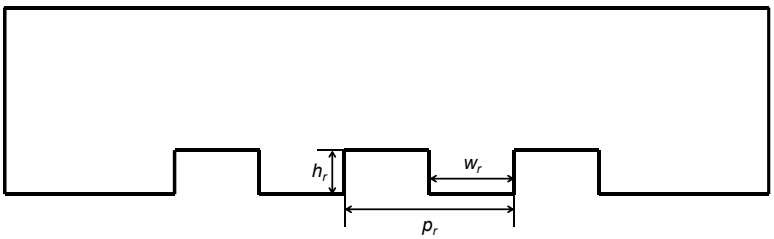

Fig. 7. Profile of relay grating, which is a rectangular or binary grating. h_r is the grating height, p_r the grating period, and w_r the grating width.

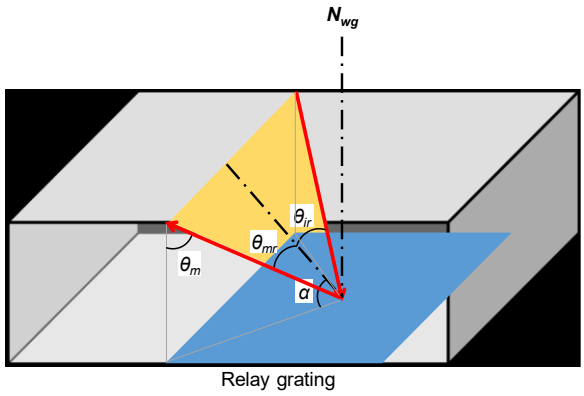

Fig. 8. Geometry of incident angle θ_{ir}, diffraction angle θ_{mr} of mth order, and waveguide normal N_{wg}. The azimuthal angles of incident and diffracted fields differ by the angle α and the plane of incidence is inclined by the angle θ_m relative to waveguide normal N_{wg}.

2.9. Out-coupling grating

Out-coupling grating, as shown in Fig. 9, can be deemed as the conjugate of in-coupling grating for it would counteract the in-coupling grating and reverse the light back to its original state. To pull this off, in-coupling and out-coupling gratings shall share the same grating period and slant angle.

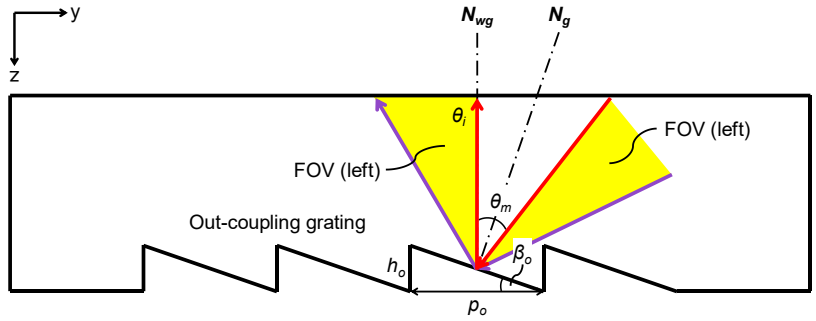

Fig. 9. Profile of out-coupling grating, which can be deemed as the conjugate of in-coupling grating for it would counteract the in-coupling grating and reverse the light back to its original state.

3. Results and discussion

3.1. Diffraction efficiency

The modeling of gratings is performed on VirtualLab Fusion (Wyrowski Photonics), which leverages the Fourier modal method [43] to rigorously compute the diffraction efficiency (DE). The design wavelength is Mercury e-line (546 nm). Dense flint glass SF6 (Schott) with a refractive index of 1.8127 at 546 nm is selected as the substrate material. Per the design rules elaborated previously, Table 5 lists the parameters for in-coupling, relay and out-coupling gratings. To ensure the uniformity across the entire eyebox, it is necessary to modulate the DEs for different exit pupils. For both in-coupling and out-coupling gratings, their efficiencies can be adjusted by the thickness of coating of aluminum. As shown in Fig. 10, DE of reflected first order (blue line of R1) increases with respect to the thickness of aluminum until it saturates after 38 nm. The efficiency of transmitted zeroth order (red line of T0), on the contrary, falls off all the way through. For the see-through AR, thin coating is recommended for out-coupling grating for the sake of

transparency. For the non-see-through VR, coating thickness can be maximized. For the relay grating, DE can be adjusted by the grating height, as shown in Fig. 11. In accordance with the scalar diffraction theory, the peak of DE occurs at 336.05 nm. Speaking of the grating fabrication, the technique may vary depending on the need. For the research, electron-beam lithography, direct laser writing, focused ion beam and holography [44] are versatile but time-consuming. For the industry, deep ultraviolet lithography and nanoimprint lithography are more suitable for mass production.

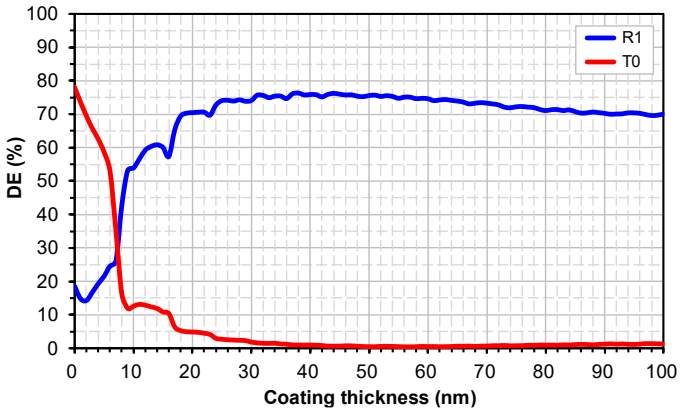

Fig. 10. DE of both in-coupling and out-coupling gratings versus the thickness of coating of aluminum. DE of reflected first order (blue line of R1) increases with respect to the thickness of aluminum until it saturates after 38 nm. The efficiency of transmitted zeroth order (red line of T0), on the contrary, falls off all the way through.

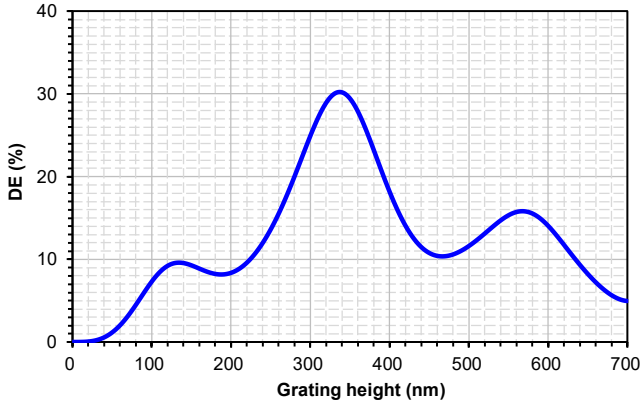

Fig. 11. DE of relay grating versus the grating height. In accordance with the scalar diffraction theory, the peak of DE occurs at 336.05 nm.

Table 5. Parameters for in-coupling, relay and out-coupling gratings.

Grating	Type	Parameter	Value
In-coupling	Blazed	p_i	545.85 nm
		h_i	164.24 nm
		β_i	16.75°
Relay	Rectangular	p_r	545.85 nm
		h_r	336.05 nm
		w_r	272.93 nm
Out-coupling	Blazed	p_o	545.85 nm
		h_o	164.24 nm
		β_o	16.75°

3.2. Field of view, eye relief and exit pupil

In the horizontal direction, as shown in Fig. 12, the yellow-highlighted region marks the intersection of left and right FOVs. The width of intersection is defined as horizontal exit pupil EP_h, which has a maximum when

$$ER = \frac{\frac{W_o}{4} - D \cdot tan\left(sin^{-1}\left(\frac{n_{air} sin\left(\frac{FOV_h}{2}\right)}{n_{wg}}\right)\right)}{tan\left(\frac{FOV_h}{2}\right)} \tag{21}$$

where ER denotes the eye relief and FOV_h the horizontal FOV. For W_o= 40 mm and FOV_h= 63°, ER= 15 mm and EP_h= 20 mm. In the vertical direction, as shown in Fig. 13, vertical exit pupil EP_v monotonically decrease as the eye relief increases, which could be formulated as

$$EP_v = H_o - 2 \cdot D \cdot tan\left(sin^{-1}\left(\frac{n_{air} sin\left(\frac{FOV_v}{2}\right)}{n_{wg}}\right)\right) - 2 \cdot ER \cdot tan\left(\frac{FOV_v}{2}\right) \tag{22}$$

where FOV_v is the vertical FOV. For H_o= 20 mm and FOV_v= 38°, EP_v= 9 mm. From the above equations, it is also important to note that, apart from the refractive index, the dimension of waveguide is another factor that keeps the expansion of FOV in check. As shown in Fig. 14, as the horizontal/vertical FOV rises to 120°, if the eye relief and exit pupil are unchanged, the required horizontal and vertical dimensions of out-coupling grating are 112 and 65 mm, respectively, somewhat impractical for wearable devices. Incidentally, as to the chromatic dispersion, the loss of FOV could be eluded by taking advantage of narrowband color scheme [45].

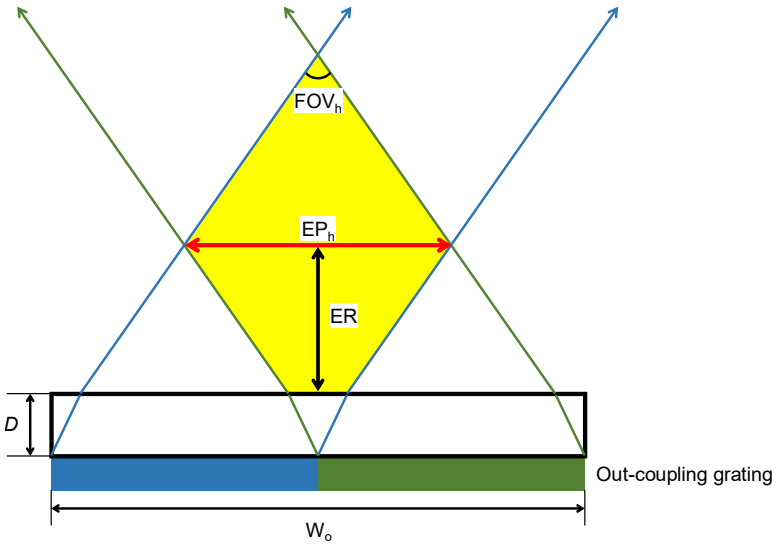

Fig. 12. Illustration of horizontal exit pupil. For W_o= 40 mm and FOV_h= 63°, ER= 15 mm and EP_h= 20 mm.

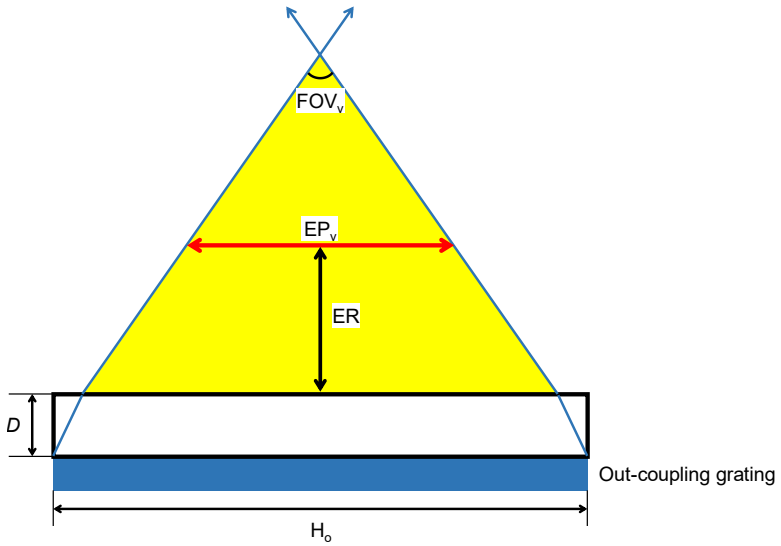

Fig. 13. Illustration of vertical exit pupil. For H_o= 20 mm, ER= 15 mm, and FOV_v= 38°, EP_v= 9 mm.

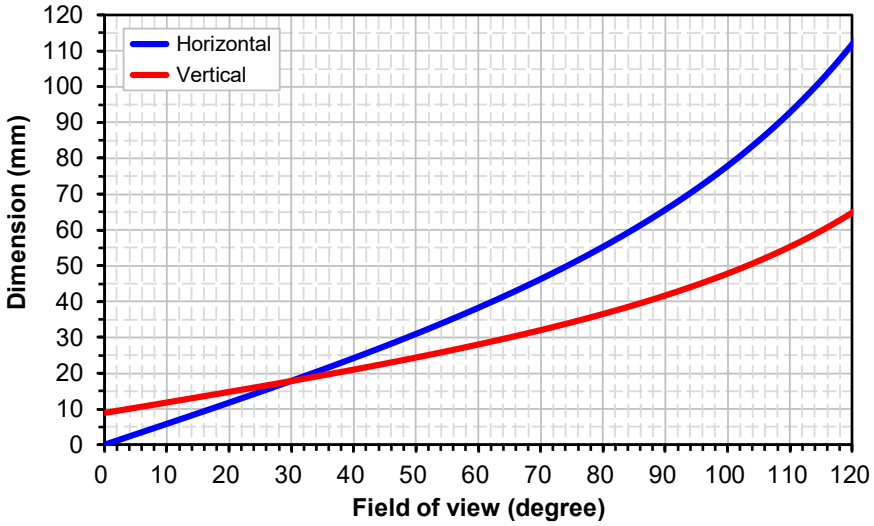

Fig. 14. As the horizontal/vertical FOV rises to 120°, if the eye relief and exit pupil are unchanged, the required horizontal and vertical dimensions of out-coupling grating are 112 and 65 mm, respectively.

3.3. Modulation transfer function

The imaging performance is quantitatively analyzed with Code V (Synopsys). Whereas Code V is a ray-tracing-based tool, it could handle the diffraction gratings with the scalar diffraction theory. Fig. 15 outlines the optical surfaces being engaged in the simulation. The optical path is arranged in the backward direction as the object—*i.e.* the virtual image of microdisplay—is located at the infinity. Waveguide is defined by surfaces 1 and 2, the diffractive properties of which are assigned as linear blazed gratings with ±1 orders, respectively. Collimating lens is defined by surfaces 3, 4 and 5. Prior to the optimization, radii of curvature of surfaces 3 and 4 and thicknesses of surfaces 3, 4 and 5 are set as variables. For the optimization, the error function is transverse ray aberration and the constraint is to target the effective focal length to be 12.7 mm. After the optimization, the final parameters are automatically tweaked as in Table 6. As shown in Fig. 16, modulation transfer function (MTF) is calculated as a function of the spatial frequency in

cycle/degree for the fields of 0° (central) and 35° (tangential and radial). At 30 cycle/degree—corresponding to the benchmark of 20/20 vision [46]—MTFs of all fields are above 0.591.

Table 6. Parameters of optical surfaces used in Code V.

Surface	Surface type	Radius (mm)	Thickness (mm)	Medium	Diffractive property
object (image)	sphere	infinity	infinity	air	n/a
1 (waveguide)	sphere	infinity	3.0200	SF6	linear grating (blazed)
2 (waveguide)	sphere	infinity	0.1000	air	linear grating (blazed)
3 (collimating lens)	asphere	6.2362	0.7679	K7	n/a
4 (collimating lens)	asphere	−29.9965	0.3800	F2	n/a
5 (collimating lens)	sphere	infinity	11.9357	air	n/a
image (microdisplay)	sphere	infinity	0.0000	air	n/a

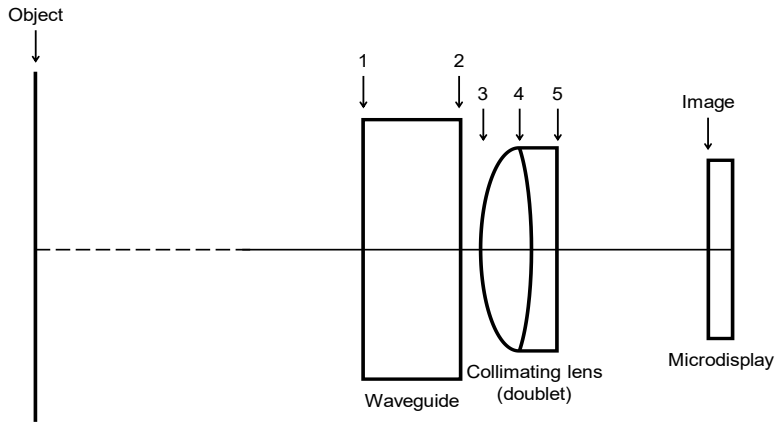

Fig. 15. Optical surfaces being engaged in the simulation. The optical path is arranged in the backward direction as the object—*i.e.* the virtual image of microdisplay—is located at the infinity. Waveguide is defined by surfaces 1 and 2, the diffractive properties of which are assigned as linear blazed gratings with opposite orders. Collimating lens is defined by surfaces 3, 4 and 5.

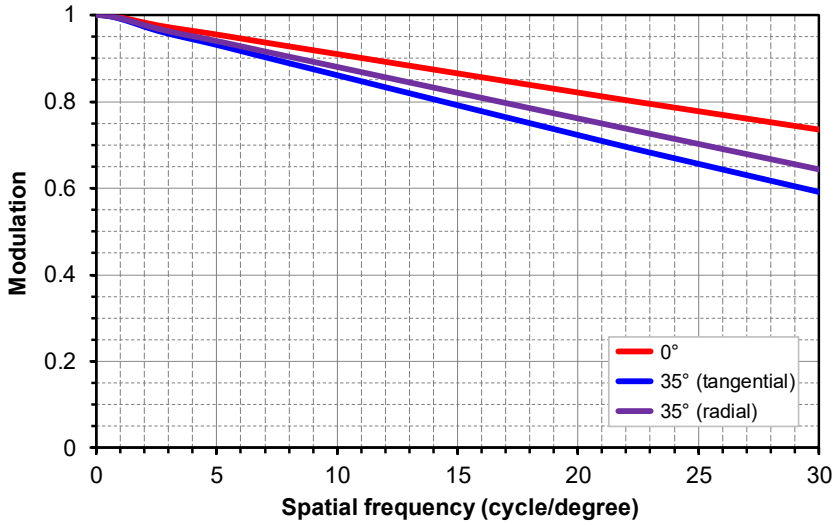

Fig. 16. MTFs calculated as a function of the spatial frequency in cycle/degree for the fields of 0° (central) and 35° (tangential and radial). At 30 cycle/degree, MTFs of all fields are above 0.591.

3.4. *Contrast ratio*

Contrast ratio hinges on the MTF of optical system as well as CR of microdisplay CR_m as [47]

$$CR = \frac{CR_m+1+MTF\cdot(CR_m-1)}{CR_m+1-MTF\cdot(CR_m-1)} \tag{23}$$

As the resolution is 1920 × 1080 and FOV= 70°, the spatial frequency is 15.74 cycle/degree. Revisiting Fig. 16, for the field of 0°, MTF= 0.858. Hence, CR= 13 (CR_m= 100,000).

3.5. *Distortion*

Distortion—the displacement of image height or ray location—is graphed in Fig. 17, from which it can be seen that the distortion up to the field of 35° is 1.38%.

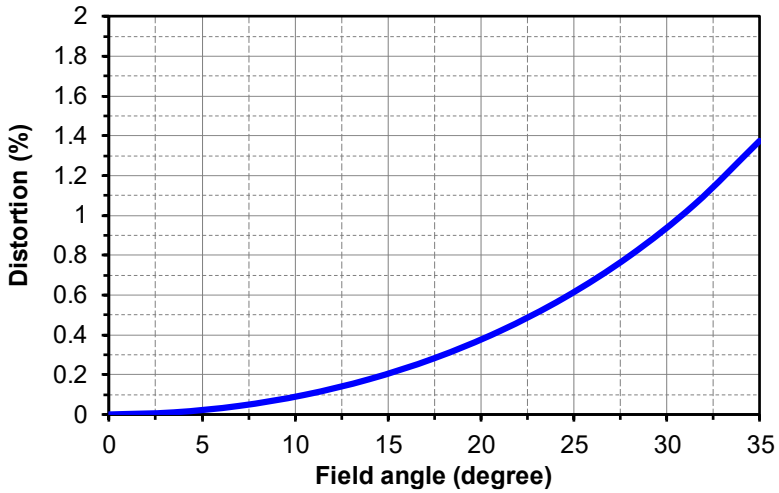

Fig. 17. Distortion calculated with respect to the field angle. It can be seen that the distortion up to the field of 35° is 1.38%.

3.6. *Simulated imaging*

Fig. 18 shows the original image alongside the virtual image. Compared to the original one, the virtual image has a mild pincushion distortion and noticeably reduced brightness at large field angles.

Fig. 18. (a) Original image (photographer: C. P. Chen, location: Kalajun Grassland, Xinjiang, China), and (b) virtual image.

4. Conclusions

A waveguide-based NED with a dual-channel EPE and design rules thereof have been comprehensively investigated. Unlike the existing EPEs, which do not split [29,31] or partially split [30] the FOV, our dual-channel EPE fully (or evenly) splits the FOV into two halves. By doing so, the upper limit of FOV can be significantly hiked. The refractive index and dimension of waveguide are identified as two factors that limit the FOV. In what follows, its key specifications are recapitulated. FOV is 70° (diagonal), eye relief is 15 mm, exit pupil is 20×9 mm^2, MTF is above 0.591 at 30 cycle/degree, CR is 13, and distortion is 1.38%. As the major glass vendors—*e.g.* Schott [48] and Corning [49]—are ambitious in pushing the envelope of refractive index of glass, the waveguide-based NED would possibly become the ultimate optical solution for both AR and VR.

Funding

This work is supported by National Natural Science Foundation of China [61901264, 61831015]; Science and Technology Commission of Shanghai Municipality [19ZR1427200, 1801H163000, 1701H169200]; and Shanghai Rockers Inc. [15H100000157].

CRediT authorship contribution statement

Chao Ping Chen: Conceptualization, Methodology, Software, Formal analysis, Resources, Writing - review & editing, Visualization, Supervision. **Lantian Mi:** Formal analysis, Investigation. **Wenbo Zhang:** Validation, Writing - original draft. **Jiaxun Ye:** Investigation, Data curation. **Gang Li:** Project administration, Funding acquisition.

Declaration of competing interest

The authors declare that they have no known competing financial interests or personal relationships that could have appeared to influence the work reported in this paper.

Acknowledgments

Special thanks to Bernard Kress (Microsoft) for his enlightenments amid the SPIE AR|VR|MR 2020 in San Francisco.

References

1. PricewaterhouseCoopers, Seeing is believing. https://www.pwc.com/gx/en/industries/technology/publications/economic-impact-of-vr-ar.html (accessed 14 January 2021).
2. J.E. Melzer, K. Moffitt, Head-Mounted Displays: Designing for the User, McGraw-Hill, New York, 1997.
3. W. Barfield, Fundamentals of Wearable Computers and Augmented Reality, second ed., CRC Press, Boca Raton, 2016.
4. B.C. Kress, Optical Architectures for Augmented-, Virtual-, and Mixed-Reality Headsets, SPIE, Bellingham, 2020.
5. J.P. Rolland, Wide-angle, off-axis, see-through head-mounted display, Opt. Eng. 39 (2000) 1760–1767.
6. L. Zhou, C.P. Chen, Y. Wu, Z. Zhang, K. Wang, B. Yu, Y. Li, See-through near-eye displays enabling vision correction, Opt. Express 25 (2017) 2130–2142.
7. C. Hong, S. Colburn, A. Majumdar, Flat metaform near-eye visor, Appl. Opt. 56 (2017) 8822–8827.
8. G.-Y. Lee, J.-Y. Hong, S. Hwang, S. Moon, H. Kang, S. Jeon, H. Kim, J.-H. Jeong, B. Lee, Metasurface eyepiece for augmented reality, Nat. Commun. 9 (2018) 4562.
9. L. Mi, C.P. Chen, Y. Lu, W. Zhang, J. Chen, N. Maitlo, Design of lensless retinal scanning display with diffractive optical element, Opt. Express 27 (2019) 20493–20507.
10. Y. Amitai, Extremely compact high-performance HMDs based on substrate-guided optical element, in: SID Symposium Digest of Technical Papers, Boston, 2004, pp. 310–313.
11. T. Levola, Diffractive optics for virtual reality displays, J. Soc. Inf. Disp. 14 (2006) 467–475.
12. T. Levola, V. Aaltonen, Near-to-eye display with diffractive exit pupil expander having chevron design, J. Soc. Inf. Disp. 16 (2008) 857–862.
13. H. Mukawa, K. Akutsu, I. Matsumura, S. Nakano, T. Yoshida, M. Kuwahara, K. Aiki, A full-color eyewear display using planar waveguides with reflection volume holograms, J. Soc. Inf. Disp. 17 (2009) 185–193.
14. D. Cheng, Y. Wang, H. Hua, M.M. Talha, Design of an optical see-through head-mounted display with a low f-number and large field of view using a freeform prism, Appl. Opt. 48 (2009) 2655–2668.
15. Y. Weng, D. Xu, Y. Zhang, X. Li, S.-T. Wu, Polarization volume grating with high efficiency and large diffraction angle, Opt. Express 24 (2016) 17746–17759.
16. Y. Wu, C.P. Chen, L. Zhou, Y. Li, B. Yu, H. Jin, Design of see-through near-eye display for presbyopia, Opt. Express 25 (2017) 8937–8949.
17. Y. Wu, C.P. Chen, L. Zhou, Y. Li, B. Yu, H. Jin, Near-eye display for vision correction with large FOV, in: SID Display Week, Los Angeles, 2017, pp. 767–770.
18. J. Ha, J. Kim, Augmented reality optics system with pinpoint mirror, US Patent 2019/0204600 A1 (2017).
19. Z. Shi, W.T. Chen, F. Capasso, Wide field-of-view waveguide displays enabled by polarization-dependent metagratings, Proc. SPIE 10676 (2018) 1067615.
20. J. Xiao, J. Liu, J. Han, Y. Wang, Design of achromatic surface microstructure for near-eye display with diffractive waveguide, Opt. Commun. 452 (2019) 411–416.
21. K. Yin, H.-Y. Lin, S.-T. Wu, Chirped polarization volume grating with ultra-wide angular bandwidth and high efficiency for see-through near-eye displays, Opt. Express 27 (2019) 35895–35902.
22. C. Yoo, K. Bang, M. Chae, B. Lee, Extended-viewing-angle waveguide near-eye display with a polarization-dependent steering combiner, Opt. Lett. 45 (2020) 2870–2873.
23. W. Zhang, C.P. Chen, H. Ding, L. Mi, J. Chen, Y. Liu, C. Zhu, See-through near-eye display with built-in prescription and two-dimensional exit pupil expansion, Appl. Sci. 10 (2020) 3901.
24. R.B. Sprague, Method and apparatus to process display and non-display information, US Patent 8,520,309 B2, 2008.
25. R. Sprague, A. Zhang, L. Hendricks, T. O'Brien, J. Ford, E. Tremblay, T. Rutherford, Novel HMD concepts from the DARPA SCENICC program, Proc. SPIE 8383 (2012) 838302.
26. Y. Wu, C.P. Chen, L. Mi, W. Zhang, J. Zhao, Y. Lu, W. Guo, B. Yu, Y. Li, N. Maitlo, Design of retinal-projection-based near-eye display with contact lens, Opt. Express 26 (2018) 11553–11567.
27. S. Lan, X. Zhang, M. Taghinejad, S. Rodrigues, K.-T. Lee, Z. Liu, W. Cai, Metasurfaces for near-eye augmented reality, ACS Photonics 6 (2019)864–870.

28. J. Chen, L. Mi, C.P. Chen, H. Liu, J. Jiang, W. Zhang, Design of foveated contact lens display for augmented reality, Opt. Express 27 (2019) 38204–38219.
29. B.C. Kress, W.J. Cummings, Optical architecture of HoloLens mixed reality headset, Proc. SPIE 10335 (2017) 103350K.
30. T. Vallius, J. Tervo, Waveguides with extended field of view, US Patent 9,791,703 B1, 2016.
31. B.T. Schowengerdt, D. Lin, P. St. Hilaire, Multi-layer diffractive eyepiece, US Patent 2018/0052277 A1, 2017.
32. D. Grey, S. Talukdar, Exit pupil expanding diffractive optical waveguiding device, US Patent 10,359,635 B2, 2018.
33. J.D. Waldern, S. Abraham, M.M. Popovich, DigiLens holographic photopolymers for wide angle AR waveguides, Proc. SPIE 11367 (2020) 113670O.
34. Wikipedia, Spherical coordinate system. https://en.wikipedia.org/wiki/Spherical_coordinate_system (accessed 14 January 2021).
35. E.G. Loewen, E. Popov, Diffraction Gratings and Applications, Marcel Dekker, New York, 1997.
36. D. Armitage, I. Underwood, S.-T. Wu, Introduction to Microdisplays, Wiley, Hoboken, 2006.
37. Sony Semiconductor Solutions Group, OLED microdisplay. https://www.sony-semicon.co.jp/e/products/microdisplay/oled/product.html (accessed 14 January 2021).
38. J. Yang, W. Liu, W. Lv, D. Zhang, F. He, Z. Wei, Y. Kang, Method of achieving a wide field-of-view head-mounted display with small distortion, Opt. Lett. 38 (2013) 2035–2037.
39. R.E. Fischer, B. Tadic-Galeb, P.R. Yoder, Optical System Design, second ed., McGraw-Hill Education, New York, 2008.
40. F.L. Pedrotti, L.M. Pedrotti, L.S. Pedrotti, Introduction to Optics, third ed., Pearson, London, 2006.
41. D.C. O'Shea, T.J. Suleski, A.D. Kathman, D.W. Prather, Diffractive Optics: Design, Fabrication, and Test, SPIE, Bellingham, 2004.
42. D.A. Pommet, M.G. Moharam, E.B. Grann, Limits of scalar diffraction theory for diffractive phase elements, J. Opt. Soc. Am. A 11 (1994) 1827–1834.
43. L. Li, New formulation of the Fourier modal method for crossed surface-relief gratings, J. Opt. Soc. Am. A 14 (1997) 2758–2767.
44. C.P. Chen, Y. Su, C.G. Jhun, Recent advances in holographic recording media for dynamic holographic display, J. Opt. Photonics 1 (2014) 1–8.
45. C.P. Chen, Y. Li, Y. Su, G. He, J. Lu, L. Qian, Transmissive interferometric display with single-layer Fabry-Pérot filter, J. Disp. Technol. 11 (2015) 715–719.
46. J. Chen, L. Mi, C.P. Chen, H. Liu, J. Jiang, W. Zhang, Y. Liu, A foveated contact lens display for augmented reality, Proc. SPIE 11310 (2020) 1131004.
47. C.P. Chen, L. Zhou, J. Ge, Y. Wu, L. Mi, Y. Wu, B. Yu, Y. Li, Design of retinal projection displays enabling vision correction, Opt. Express 25 (2017) 28223–28235.
48. Schott, High refractive index wafers for augmented reality. https://www.us.schott.com/advanced_optics/english/applications/augmented-reality.html (accessed 14 January 2021).
49. Corning, Precision glass wafers. https://www.corning.com/worldwide/en/products/advanced-optics/product-materials/PrecisionGlassSolutions.html (accessed 14 January 2021).